An Autoinhibited Conformation of the DnaB-Replicative Helicase – phage λP Loader Complex

*Dhanjai Brown[1,2], *Abhipsa Shatarupa[1,2], Paul Dominic B. Olinares[5], Jillian Chase[1,2], Eta Isiorho[6], Brian T. Chait[5], and David Jeruzalmi[1,2,3,4#]

[1]Department of Chemistry and Biochemistry, City College of New York, New York, NY 10031, USA.

Ph.D. Programs in Biochemistry[2], Biology[3], and Chemistry[4], The Graduate Center of the City University of New York, New York, NY 10016, USA.

[5]Laboratory for Mass Spectrometry and Gaseous Ion Chemistry, The Rockefeller University, New York, New York 10065, USA

[6]Structural Biology Initiative, CUNY Advanced Science Research Center, New York, NY 10031, USA

#For correspondence: dj@ccny.cuny.edu

*These authors contributed equally.

Abstract

Replicative helicases are closed protein rings and require loader proteins for assembly on DNA at origins of DNA replication. Multiple copies of the bacterial DnaC or the phage λP loader proteins bind to the closed planar ring of the DnaB replicative helicase and trigger its reconfiguration into an open spiral conformation wherein an internal chamber becomes accessible for entry to physiologically produced single stranded DNA at the replication origin. Although a great deal was learned from a previously determined cryo-EM structure of the *E. coli* DnaB helicase bound to the phage helicase loader λP (BP), the pentameric λP ensemble was not well resolved and this stymied deeper insights. We revised have the BP structure using X-ray and AlphaFold determined structures to interpret a 2.8Å cryo-EM density map. We find that the λP ensemble adopts a profoundly asymmetric configuration; one copy of λP, which is visualized in full, binds at the top and bottom of the open DnaB spiral; presence of a single breach in the DnaB open spiral means that the remaining four copies of λP must adopt distinct, and currently unknown, conformations. Although DnaB's internal chamber remains accessible to entry of ssDNA, the λP protomer whose binding site spans the breach effectively blocks the path into the inner chamber and gives rise to an autoinhibited configuration for the BP complex. Comparisons of the λP and DnaC bound complexes of the DnaB helicase shed new light on how the two loaders, though unrelated in sequence or structure, converged on the same ring-opening mechanism. The autoinhibited conformation of the BP complex suggests structural changes that must accompany recruitment to the initiator protein complex at the replication origin.

Introduction

Replicative helicases, and the loader proteins that assemble them onto DNA, are found in the chromosomal replicating systems from all cellular domains of life [1–3]. Replicative helicases are oligomeric entities that circumscribe an inner chamber into which single-stranded DNA (ssDNA) is loaded. Given that DNA is effectively an infinitely long polymer with no free ends, assembly of replicative helicases on DNA requires the activity of specialized loader proteins; assembly takes place during the initiation phase of DNA replication. In bacteria, the replicative helicase, termed DnaB in most bacteria (henceforth: DnaB) or DnaC in *B. subtilis*, is a homohexamer that encircles and translocates on the lagging strand at the replication fork, while excluding the second strand from the inner chamber; ATP-dependent translocation by DnaB mediates separation of duplex DNA into templates for replication. An extensive body of literature has described several helicase loaders in bacteria, including *E. coli* DnaC, bacteriophage λP, DnaI from *B. subtilis*, and the DciA/DopE family [4–9].

The DnaB hexameric helicase is a two-tiered, ring-shaped ensemble with an internal chamber that is ordinarily sealed to entry by ssDNA [10–12]. Each DnaB protomer is formed out of two domains connected by a 'linker helix' element (LH). Pairs of amino-terminal (NTD) domains engage in a dimeric arrangement and three of these dimers assemble into a trimeric configuration that represents one of DnaB's layers; the NTD layer circumscribes the DNA binding channel and provides binding sites for DNA primase during the elongation phase of DNA replication. The second of DnaB's layers is formed out of six carboxy-terminal domains (CTD), which, in contrast to the NTD layer, exhibits a pseudo-sixfold

arrangement. Each CTD provides three residues for contacts to the phosphate backbone of ssDNA within the inner chamber of DnaB [13]. The NTD and CTD layers are found in two arrangements, termed: dilated and constricted; these states have differently sized inner chambers that are determined by distinct inter-subunit contacts. The NTD and CTD sub-domains of each DnaB subunit are linked by an LH element, which, in the hexameric assembly, packs against the docking helix (DH) of an adjacent DnaB subunit [10–12].

Loading of the bacterial DnaB helicase onto origin DNA occurs at the nexus of two pathways that first assemble two sub-complexes; these two sub-complexes, then, coalesce, into the complete initiation complex at the replication origin [14–16]. The first sub-complex to be formed is the oligomeric initiator protein complex (*E. coli:* DnaA or phage λ: O) at the cognate replication origin; a critical outcome that emerges out of this complex is initial melting of the origin's DNA unwinding element (DUE). The second sub-complex is assembled by capture and remodeling of the DnaB helicase by the helicase loader. These two pathways converge with delivery of the loader-bound helicase to the origin; ssDNA produced by the initiator – origin DNA complex is proposed to enter the opened inner chamber of DnaB. A series of additional binding and remodeling events culminate in assembly of the replication fork.

In bacteria, two schemes, termed: ring-breaking or ring-making, have been reported to explain mechanisms of helicase loading [17, 18]. Ring-breaking features stabilization of a form of hexameric DnaB wherein one interface is breached; *E. coli* DnaC and bacteriophage λP are ring-breakers. In the ring-making

scheme, the active helicase is assembled by the loader on DNA out of individual DnaB subunits; *B. subtilis* DnaI loader is reported to operate as a ring-maker [5].

Here, we focus on the ring-breaking loaders where the binding and remodeling events associated with loading and activating the DnaB helicase can also be considered to transition through four stages [10–13, 19–21]. The isolated stage I helicase adopts a closed planar configuration with the NTD and CTD layers either in the dilated or constricted shape. In stage II, DnaB has been captured and remodeled by the loader (*E. coli:* DnaC or phage λ: P) into an open right-handed spiral, with both tiers in the constricted conformation [19, 21, 22]. Remodeling creates openings in DnaB's two tiers sufficient in size to permit access to the inner chamber by ssDNA. The ATPase and translocase activities of DnaB are suppressed when bound by the loader [56,58,69–71]. Engagement with initiator-produced ssDNA by the helicase•loader complex leads to stage III; ssDNA is bound by both the loader and within DnaB's now topologically closed inner chamber; the CTD tier features the constricted state, while the NTD layer is dilated [19]. Expulsion of the loader accompanies transition to stage IV, which is suggested to be the translocating form of DnaB [13, 19].

Structure analysis of the *E. coli* DnaB helicase bound in distinct complexes to the *E. coli* DnaC (BC) and phage λP (BP) shed considerable light on mechanisms of helicase opening, ssDNA entry, followed by sealing of the inner chamber of DnaB with ssDNA trapped inside [19, 21, 22]. Although unrelated in sequence or structure, the two loaders feature a similar overall architecture: a globular domain attached to an element termed the lasso/grappling hook. Differing

numbers of loader subunits (DnaC: 6; λP: 5) in the BC and BP complexes engage the CTD layer of DnaB to trigger the change from the closed planar to a closely related open spiral configuration. Remarkably, one of the only regions of structural resemblance between the two loaders is the alpha helix at the tip of the lasso/grappling hook that is positioned between the LH and DH helices of two adjacent DnaB subunits. Amazingly, however, the protein chain direction of these elements (λP: C-N; DnaC: N-C) differs, implying that chain direction is not important for triggering helicase opening. This unusual feature of λP and DnaC reflects a type of molecular mimicry that emerged from convergent evolution.

Analysis of the structure of the BP complex by cryogenic-electron microscopy (cryo-EM) at 4.1 Å provided a great deal of insights into helicase loading, however, the limited resolution obscured the full structure of the λP loader as only the carboxy-terminal domains of the five protomers were visible in the EM map. We have extended the resolution of our EM analysis to 2.8 Å. Using a combination of X-ray crystallography and AlphaFold calculations, we revised the structures of the five carboxy-terminal domains (domains III/IV, lasso/grappling hook). The AlphaFold model also enabled the complete structure one λP monomer to be completely positioned within the BP complex; unexpectedly, this monomer binds across the breach in the CTD tier. Thus, although the NTD and CTD tiers of DnaB retain their openings, disposition of one λP loader seals the entrance and creates a previously unrecognized autoinhibited conformation of BP. We discuss implications for the complete ensemble at the origin of both the autoinhibited form of BP and the radical asymmetry exhibited by the five-

membered λP ensemble whereby one of its constituent subunits adopts a unique conformation that cannot be adopted by any of the other four.

Results

Complete Structure of the λP Helicase Loader

Analysis of the 4.1 Å cryo-EM (EM) density map (EMDB: 7076) of the BP complex provided considerable insight into helicase opening and loading [21]. Although a complete model for the DnaB helicase could built into the EM map, only the carboxy-terminal domains of λP could be visualized, but without the crucial mapping of amino acid sequence to structure. Moreover, a lower-resolution portion of the EM map, likely corresponding to one of the five amino-terminal domains of λP, could not be fully interpreted. Lack of a model for the complete structure of the λP helicase loader stymied deeper understanding of mechanisms of bacterial helicase loading. Furthermore, poor solubility of λP complicated these and prior efforts to understand its overall architecture.

To overcome these deficiencies, we applied protein engineering and experimental structural analysis and AlphaFold [23, 24] structure prediction to define the complete structure of λP. Using the structure of λP within the BP complex (PDB = 6BBM, [21]) as a guide, we isolated a soluble fragment of λP (residues 105 to 210) and determined its X-ray crystal structure (residues 119 to 192) at 1.86 Å (Figure 1). The resulting structure revealed a three-helix structure resembling that seen in the earlier cryo-EM analysis; further the crystal structure confirmed prior inferences about λP's protein chain direction and the approximate side chain mappings to the structure.

The AlphaFold calculation provided five predicted conformers of λP; each conformer harbored four domains: two compact domains (domain II: residues ~30 to ~119; domain III: residues ~120 to ~192) and two flexibly linked structural domains at the amino (residues 1 to ~30) and carboxy (193 to 233) termini with a single alpha helix, termed the N-terminal and C-terminal lasso/grappling hooks (Figure 1). The carboxy-terminal domain of λP and its associated lasso (domains III/IV) had been first described in the EM analysis of the BP complex [21], although the relative position of these two structural elements differs considerably between the experimental EM map and the AlphaFold predicted structure. The crystal structure of λP domain III superimposed well on the AlphaFold predicted structure (root mean square deviation (RMSD) of 0.328 Å over 478 atoms). AlphaFold predicted a four helical bundle for the amino terminal domain (domain I/II) that terminated in a lasso-like amino-terminal helix. Notably, the AlphaFold predicted conformers hints at flexibility in the arrangement of the four domains.

The 2.8 Å Cryo-EM Structure of the *E. coli* DnaB – λP helicase Loader

The goal of this work had been to obtain a cryo-EM structure of the BP complex bound to ssDNA. Although the native mass spectrometry revealed clear presence of a BP-ssDNA species, the 2.8 Å map that we obtained did not contain ssDNA. However, the EM maps that we did obtain were of higher resolution than our prior study [21] and revealed the complete structure of one of the five copies of the λP loader (Figure 2, chain Z) and clarified the interface between helicase and loader, as it confirmed findings about the right-handed open spiral configuration of the DnaB helicase [21, 22]. The crystal structure of λP domain III could be unambiguously positioned into each copy of the loader in our map. In the

revised BP complex (Figure 2), five domains III/IV of the λP loader ensemble bind at DnaB subunit interfaces; notably, the C-terminal helix of each monomer, now termed the C-terminal lasso/grappling hook, binds DnaB at a site formed out of the LH and DH elements. Density corresponding to the amino-terminal domains I/II (1-118) of one copy of λP (chain Z), which had been poorly resolved in our earlier study [21], was sufficiently ordered to allow fitting of the model calculated by AlphaFold. No density was observed for the amino-terminal domains of λP chains V, W, X, and Y), and, so, their structure and function are not revealed in the current work. Notably, the configuration of the four λP domains in AlphaFold calculated structures did not match that seen in our EM maps, as such, considerable adjustment of the AlphaFold calculated structure was required for fitting into our map. The amino-terminal domain I, termed the N-terminal lasso/grappling hook, binds to the DH element at the breached DnaB interface; the partner LH element of this interface is not seen in our EM maps. However, the geometry of the interaction made by the N-terminal lasso with the DH element at the breach diverges considerably from that made by the C-terminal lasso with the LH-DH elements. Our map also showed features that may correspond to one additional amino-terminal domain belonging to λP chain Y.

The DnaB hexamer in the revised model of the BP complex features a very similar configuration to that seen in the earlier analysis. In comparison, to the closed planar constricted form of DnaB, both the CTD and NTD layers feature similar helical pitch, rise, and twist parameters that closely follow those seen in the earlier model. Distortions in the hexamer that accompany transition from the

closed planar (Stage I) to right-handed open spiral breach in one of the six DnaB interfaces (Stage II), on both the NTD and CTD tiers, to create openings of the appropriate size to admit ssDNA into the inner chamber.

The Amino-Terminal Domains (I/II) of One Copy of the λP Loader Seals DnaB's Internal Chamber

Two aspects of the finding of the complete structure of one (of five) λP loader molecules are remarkable. First, unlike the other four copies, λP chain Z features an ordered amino-terminal domain (domains I/II). λP chain Z also contacts three DnaB subunits (chains B, A, and F). Notably, DnaB chains A and B are at either side of the breach, therefore, the space occupied by λP chain Z spans the breach (The other four λP chains each contact two subunits). As such, even though openings in the NTD and CTD tiers of the open spiral DnaB conformation provide entrances for ssDNA, the disposition of chain Z of λP seals the entry to a physiological ssDNA substrate at a replication origin**.** Furthermore, the finding that one copy of λP seals the entrance to the inner chamber of DnaB implies that the BP complex represents a previously undescribed autoinhibited conformation during assembly of the replicative helicase at the phage origin, and, therefore, mechanisms must exist that mediate opening of the path into DnaB's inner chamber. Second, in the BP complex, it is now clear that the five subunit λP ensemble will be radically asymmetric. The presence of a single breach in DnaB implies that only one copy of the ensemble can populate the configuration adopted by λP chain Z; the rest must necessarily feature different configurations and play different roles during replication initiation. Notably, these two features distinguish

the λP ensemble from the DnaC loader, which is neither asymmetric, nor does it impede entry of ssDNA into the inner motor chamber [19].

Comparison of the λP ensemble in the revised BP model with the BC complex reveals how the two loaders have converged on the same solution to open the closed planar form of DnaB. Superposition of the two complexes on the CTD of the DnaB subunits at the bottom of the spiral (in the pose in Figure 2) reveals that the two loaders share two common elements (Figure 3). First, as noted previously [22], the five λP and the six DnaC monomers position the lasso helix at a nearly equivalent locations at each LH-DH junction, albeit with divergent protein chain directions. Both complexes feature an open spiral DnaB with a breached interface. One of the six DnaC monomers (at the top of the spiral) positions the lasso adjacent to the DH element; the LH element of the breached interface of the BC complex has migrated to the bottom of the spiral. Second, we were surprised to find that N-terminal lasso/grappling hook of λP chain Z positions the amino terminal helix of this element against the DH helix of DnaB chain B at the top of the spiral; notably, the position of the N-terminal lasso overlaps with, but is distinct from, the DnaC lasso/grappling hook that is bound to the same site (Figure 3). For both loaders, positioning of cognate elements on DnaB chain B at the top of the spiral has the effect of sterically suppressing closure of the clamp to the closed planar configuration. Interestingly, then, λP chain Z uses its carboxy-terminal lasso to contribute to breaching the interface by contacting DnaB subunits A and F at the bottom of the spiral <u>and</u> its amino-terminal lasso to contact DnaB subunit B, thereby, preventing ring-closure. In other words, elements of one λP

molecule (chain Z) overlap with those of two DnaC molecules (chain G and chain L in PDB entry: 6QEL) leading us to speculate that perhaps the functions of the two DnaC chains noted above are subsumed into one chain of the λP ensemble. In this context, it is noteworthy that λP's higher affinity to DnaB, which can displace DnaC from the BC complex [25], may be explained by the multitude of contacts to DnaB made by λP chain Z.

The Carboxy-terminal Domain of the λP Ensemble Shears the LH-DH Interface

Comparison of the open-spiral DnaB in the BC complex [19] and the BP complex [22] against the closed planar form suggested that the DnaC and λP loaders disrupt the interaction between the LH and DH helices that come together from adjacent DnaB subunits in the hexamer. Here, we superimposed the B_2P_1 sub-structures of the revised BP complex on the CTD of DnaB chain A (residues 206 to 471 and excluding the LH (residues 181:196) and DH helices (residues 290:306)) at the bottom of the spiral in the pose in Figures 2 and 4 and obtained root mean square deviations of 0.61 to 0.67 Å on 246 Cα atoms (Figure 4). We found that, although not included in the superposition, the second CTD DnaB in the B_2P_1 sub-structure and domain III/IV of the λP superimpose well; this suggests that a relatively rigid DnaB-CTD_2- λP substructure. The LH and DH helices of each of the five B_2P_1 sub-structures are found to be rotated outward away from the central chamber, and, within the error of our coordinates, the outward rotations were the same in each instance. The sixth LH-DH species in DnaB (top and bottom of spiral as in the pose in Figure 2) is entirely disrupted as the underlying subunit interface is disrupted; indeed, the sixth LH helix is not seen in our EM maps. The

radical asymmetry of the λP ensemble is limited to the amino-terminal domains (I/II), which adopt at least two different configurations: chain Z seals the breach in DnaB and chain V, W, X, and Y feature a second, distinct, and a yet unknown, conformation; the carboxy-terminal domains (III/IV) deploy a common configuration. Taken together, we find that binding of the pentameric λP ensemble deploys five carboxy-terminal helices to remodel the LH-DH interaction of five consecutive DnaB subunit interfaces; remodeling triggers shift from the closed planar to the open spiral form of DnaB.

Discussion

X-ray crystallography, AlphaFold calculations, and a 2.8 Å cryo-EM map were used to revise the model of the *E. coli* DnaB – λP helicase loader complex. The 1.86 Å crystal structure of λP domain III and an AlphaFold calculated structure of the complete structure of λP greatly enabled interpretation of a 2.8Å cryo-EM map that we calculated. In the revised model, configuration of right-handed open spiral of DnaB within the BP complex closely followed that of our earlier analysis.

The revised BP model revealed a radically asymmetric configuration for the λP ensemble. A single λP monomer (chain Z) was found to span the breach in the DnaB open spiral. In addition to the interactions to adjacent DnaB subunits (chain A and F) made by the C-terminal linker/lasso domains (III/IV), seen in the prior structure, the N-terminal domains also contact a third DnaB subunit (chain B) across the breached interface; this contact involves the N-terminal lasso element which packs against the DH helix at the breached interface. This novel interaction could serve to block reclosure of DnaB to the closed planar form. Although the two tiers of open-spiral form of DnaB maintain external access to the internal chamber,

the combination of contacts by the N-terminal and C-terminal domains of λP-chain Z preclude entry of physiological ssDNA into the inner chamber.

The C-terminal domains of the remaining four protomers (chains V, W, X, and Y) of λP are found in configurations closely related to those in our earlier structure [21]; the N-terminal domains of these chains remain poorly ordered. Binding of the five lasso/grappling hooks to LH-DH junctions has been proposed to trigger the change from the closed planar to the right-handed open-spiral form of DnaB [19, 22]. The five λP CTDs contribute to this mechanism by positioning five lasso/grappling helical elements (domain IV) at the LH-DH junctions; these interactions force the LH and DH helices to rotate outward away from the inner chamber. The current structure suggests no difference in configuration between the five instances of the lasso helix-LH-DH-sub-structure, leaving unanswered the question of how the breaching of the single cracked interface of DnaB is specified.

Asymmetry in the configuration of the five protomers of the λP ensemble provokes questions about mechanisms that mediate helicase opening and ssDNA loading at the origin. λP chain Z leverages its N-terminal and C-terminal lasso domains to span the DnaB breach by contacting the DH element at the breach and the LH-DH junction at the bottom of the DnaB spiral. λP chain Z appears to harbor the elements (e.g., N- and C-terminal lasso/grappling hooks) needed to open the closed planar form of DnaB on its own; if so, what mechanisms are implemented by the C-terminal lassos of the other λP chains? Furthermore, disposition of λP chain Z amino-terminal domain (I/II) across the breached DnaB interface creates an autoinhibited conformation of the BP complex wherein access by physiological

ssDNA to the inner chamber is precluded. How is this autoinhibition relieved? We speculate that the autoinhibition will be relieved as the BP complex is recruited to the pre-formed λO•Oriλ complex at the replication origin (Figure 5). Interactions between five N-terminal domains of λP, one ordered and four disordered in the autoinhibited BP complex, and the carboxy-terminal domains of λO could anchor the complex to the λO•Oriλ ensemble, while at the same time stimulating detachment and rotation of domains I/II of λP chain Z to clear the path for ssDNA into the inner chamber. Additional studies will be required to clarify mechanisms that accompany recruitment of the autoinhibited state of the BP complex to the replication origin.

Materials and methods

Constructs of the λP helicase loader

The biochemical and structural studies in this work relied upon a large set of His-tagged constructs of λP, three of which are described here. The sequence inserted for each construct was cloned into pRSFDuet vector and verified by DNA sequencing (Genewiz/Azenta). These efforts identified soluble domains corresponding to the following constructions: 105-205, 110-220, 105-210, which were utilized in biochemical studies; the construct spanning residues 105-210 provided a sample suitable for X-ray crystallographic studies.

Protein Biochemistry

The full length pET24a-EcDnaB, pCDFDuet-Lambda-P and pET24a-EcDnaB-R403A-E404A-G406 were all purified using the method detailed in [21]. λP105-210 was transformed and expressed in *E. coli* BL21 (DE3) cells. The growth parameters were like those described in [21], with the sole exception being that the induction proceeded at 16°C for 16 hours. λP105-210 substituted with

selenomethionine were prepared for X-ray crystallographic studies as described in Orlova et al [26].

Cells expressing histidine-tagged λP105-210 were lysed with a sonicator (60% amplitude; 3 min; 0.3 on, 0.6 off). Crude λP-105-210 was recovered in the lysis supernatant and further purified over NiNTA (Qiagen) pre-equilibrated with 50 mM Na-phosphate pH 7.6, 500 mM NaCl, 10% glycerol and 5 mM BME. The Ni-NTA bead with adsorbed λP-105-210 was treated with successive washes of 25 mM, 50 mM, 100 mM imidazole in the buffer above. Partially purified λP105-210 was eluted from the NiNTA column using successive washes containing 250 mM, 500 mM, and 500 mM imidazole in the above buffer. Pooled λP105-210-containing fractions were concentrated (5kDA) to 3 mg/ml and applied at a flow rate of 1ml/min onto a 320 ml Superdex200 size exclusion column (SEC) equilibrated in 100mM NaCl, 10mM Tris-HCl pH 7, 5% glycerol and 5mM BME. Fractions containing λP105-210 were concentrated to 100 μM), aliquoted to 100 μL aliquots, flash frozen in liquid nitrogen, and stored at -80°C until use.

X-ray structure determination of λP domain III (residues 105 – 210)

λP105-210 protein in this buffer: 100mM NaCl, 10mM Tris-HCl pH 7, 5% glycerol and 5mM BME was thawed on ice and further concentrated to > 200μM (~3.5 mg/ml). Crystallization trials were conducted using the RT Gryphon (Art Robbins) available at the crystallization facility of the Structural Biology Initiative at the Advanced Science Research Facility at the City University of New York. Crystals of λP105-210 were prepared using the sitting drop vapor diffusion method by mixing either 0.1, or 0.2 or 0.4 μL of the protein solution and 0.2 μL of a series of commercially available crystallization screens (Qiagen). Conditions that

provided initial hits were optimized using bespoke screens prepared at the crystallization facility. Crystals for X-ray diffraction were grown from an optimized screen consisting of 3M – 4M NaCl with 0.1M HEPES pH 7 – 8, in 7 days at room temperature (22-23°C). For X-ray diffraction, crystals >70 microns were cryoprotected by adding 0.2μL cryo-oil directly onto the crystal in the well before looping into nylon loops (>50 microns) and flash freezing in liquid nitrogen.

Diffraction data for sulfomethionine and selenomethionine λP105-210 crystals were recorded at the ID-E and ID-C (respectively) beamlines at the Northeastern Collaborative Access Team (NECAT) Center for Advanced Macromolecular Crystallography at the Advanced Photon Source at Argonne National Laboratory. Data from sulfomethionine crystals were measured using a wavelength of 0.97918 Å to Bragg spacings of 1.86 Å. Data from selenomethionine crystals were measured at 12,662 eV (Se-edge) and a wavelength of 0.97918 Å, to a Bragg spacing of 1.86 Å. Both sulfomethionine and selenomethionine λP105-210 crystallized in space group $P3_121$, with the following cell parameters: a = 49.731, b = 49.731, c = 70.772, alpha = 90°, beta = 90°, and gamma = 120°. Matthew's analysis [27] implied presence of one copy of λP105-210 in the crystallographic asymmetric unit.

Diffraction images were integrated and scaled with HKL2000 [28]. Efforts to use the sulfomethionine data set to determine the domain III structure using molecular replacement and various search models derived from the cryo-EM structure of the DnaB-λP complex did not provide a reliable solution. However, the structure was readily determined, using the single anomalous dispersion (SAD)

method as implemented in the Phenix suite [29]. The Autobuild and Refine programs in Phenix aided the development of the final model that consists of residues 119 to 192 (residues 105 to 118 and 193 to 210 could not be visualized) and featured a crystallographic R factor, $R_{working}$ of 22.58% and an R_{free} of 24.36%. In all cases, initial models were improved using several rounds of model building and refinement as implemented in Phenix [29]. Structural models were visualized with Coot [30, 31] and Pymol [32].

Native mass spectrometry (MS)

The native MS analysis of all samples (apo-BP, ssDNA-BP) was carried out at a protein concentration of 5 μM. The ssDNA constructs (Genewiz, LLC) included: (1) a 43-mer sequence (5'-TGACGAATAATCTTTTCTTTTTTCTTTTGTAATAGTGTCTTTT-3') derived from the DNA unwinding element (DUE) of Oriλ [33], and (2) a series of thymidylate homopolymers of varying nucleotide length (dT 25 nt, dT 35 nt or dT 45 nt). The protein samples were then buffer exchanged into native MS solution (450 mM ammonium acetate, pH 7.5, 0.5 mM magnesium acetate, 0.01% Tween-20) using Zeba microspin desalting columns (Thermo Scientific) with a 40-kDa molecular weight cut-off (MWCO). For samples containing ssDNA, the buffer-exchanged BP complex was incubated with nucleic acid at a molar ratio of 1:1.2 for 20 min on ice prior to native MS experiments. A 2 – 3 μL aliquot of the sample was loaded into an in-house fabricated gold-coated quartz capillary. The sample was then sprayed into an Exactive Plus EMR instrument (Thermo Fisher Scientific) using a static nanospray source. The MS parameters used are spray voltage, 1.0 – 1.4 kV; capillary temperature, 100 °C; in-source dissociation, 10 V; S-lens RF level, 200;

resolving power, 8750 at *m/z* of 200; AGC target, 0.5 – 3 × 10^6; number of microscans, 5; maximum injection time, 200 ms; injection flatapole, 8 V; interflatapole, 4 V; bent flatapole, 4 V; high energy collision dissociation (HCD), 200 V; ultrahigh vacuum pressure, 6 – 9 × 10^{-10} mbar; total number of scans, 100. The EMR instrument was mass calibrated using cesium iodide. The native MS spectra were visualized using the Thermo Xcalibur Qual Browser (version 3.0.63). Deconvolution was performed manually. The observed mass deviations from expected mass ranged from 0.04% to 0.09% due to peak broadening mainly from nonspecific magnesium adduction. All mass spectrometric data were measured by PDBO in the laboratory of BTC.

Sample Preparation for Single Particle Cryogenic Electron Microscopy

BP complex in 20 mM Na-HEPES pH 7.5, 450 mM NaCl, 2 mM DTT, 0.5 mM MgCl2, 0.2 mM ATP, and 5% glycerol was diluted in glycerol-free buffer until the glycerol concentration was ~0.25%. Synthetic single-stranded DNA oligonucleotide 5'-TGACGAATAATCTTTTCTTTTTTCTTTTGTAATAGTGTCTTTT-3' [33] was resuspended with milli-Q water. To prepare complexes for cryo-EM, protein (1.5 μM) and DNA (1.875 μM) was mixed in a 1.25 molar excess. Protein-DNA complexes were applied to ultra-gold foil grids with holey gold support and 300 mesh size (R 0.6/1,Quantifoil Micro Tools GmbH); grids were flash-frozen as described [21] and were stored in liquid nitrogen until use.

Cryo-EM Image Analysis

A total of 25,595 un-tilted movies were recorded from the BP-ssDNA (Supplementary Figure 1) complex during a 96-hour Krios session involving Titan

Krios1 (FEI, Hillsboro, Oregon), fitted with a Gatan K3 Summit (Gatan, Pleasanton, California) direct electron detector, operating at an accelerating voltage of 300 kV; the collection was managed by Leginon [34]. Single particle movies were collected at a pixel size of 1.083 Å, at a defocus range of -1 μm to -2.5 μm, at a dose rate of 25.51 $e^-/Å^2/s$ with a total exposure of 2 seconds for an accumulated dose rate of 51.01 $e^-/Å^2$. Intermediate frames were recorded every 0.05 seconds for a total of 40 frames per micrograph. Additionally, a 25° tilted data set was collected from the same grid to mitigate expected preferred specimen orientation in BP-ssDNA complex [35]; the tilted data set was measured similar imaging parameters as with the un-tilted collection.

The 25,595 un-tilted movies were divided into 4 parts for ease of computation. The movies were processed using a procedure that encompassed contrast transfer function (CTF) estimation, motion correction, and particle picking with WARP [36]. The WARP procedure was implemented with a box size of 320 pixels at 1.083 Å/px and 150 Å diameter; this procedure produced 12.2 million particles. The WARP produced particles were imported into cryoSPARC [37–39]. One fourth (26%) of the data included corrupted particles and had to be segregated from the remaining 74% of the data. Both groups were processed separately, however, even after applying the 'check for corrupt particles' in cryoSPARC, maps calculated from the combined set of particles left us with lower quality maps, especially in the λP amino-terminal domain.

The data set that included 74% of the data was 2D classified followed by ab-initio reconstruction with C1 symmetry enforced; this procedure produced

twelve classes/volumes. Three of these classes, containing 1.82 million particles, were carried forward. Template (EMD-7076 [21]) and non-template-based calculations were then applied to these particles. In the template-based method, the 3 “good” classes and 1 “bad” class from ab-initio reconstruction jobs were subjected to heterogeneous refinement in the presence of a template EMD-7076 that, in turn, produced 4 classes termed: B0, B1, B2, and B3. Homogeneous refinement and non-uniform refinement were applied to the particles in class B0 with 1.13 million particles (9.32% of the complete set of picked particles) to provide 2.88 Å and 2.84 Å maps, respectively. Processing of the B1 class with ~432K particles produced 3.62 Å map; these particles were not pursued further. The remaining two classes (B2, B3) produced “bad” volumes and were also not further pursued. The 2.84Å non-uniform refined map was sharpened with the DeepEMhancer [40] program; this procedure yielded a significantly improved density map. The global resolution of the 2.84 Å final map generated using the template-based method was calculated following the Gold Standard Fourier Shell Correlation (GSFSC) method, which applies the gold standard cut-off value of 0.143 [41, 42]. The 2.84Å DeepEMhancer enhanced map represented the highest quality map that we obtained from this data set and would be the focus of model building and refinement efforts.

In the non-template-based method, the same 3 good classes from the *ab-initio* reconstruction jobs that were used for processing using the EMD-7076-derived template were subjected to heterogeneous refinement; this procedure produced 4 classes termed: A0, A1, A2, and A3. Class A0 with 1.06 million

particles was subjected to homogeneous refinement and non-uniform refinement and produced maps with resolutions of 2.95 Å and 2.87 Å, respectively. These maps were of lower quality than the 2.84Å map produced via the template-based method and were not used further.

The tilted dataset was processed in the same manner as described above and produced a final map with a global resolution of 3.30 Å. Despite the lower resolution of the tilted (3.30 Å) map vs the un-tilted (2.84 Å), we went ahead and combined the homogeneously refined particles from the tilted and un-tilted datasets; this procedure yielded a map with a global resolution of 2.94 Å after non-uniform refinement. However, inspection of the combined map revealed a lower quality map, especially in the amino terminal domain of λP and the side-chain densities overall than the un-tilted 2.84 Å map. As such, the combined map was abandoned, and we focused our model building and refinement on the un-tilted map.

Model building and refinement

The previously described BP model (PDB: 6BBM) was positioned into the 2.84 Å EM map using Molrep [43–46] . Five copies of the 1.86Å λP domain III could be reliably positioned in the EM map. We calculated the complete model of λP with the Google CoLab implementation of AlphaFold in ChimeraX [23, 24, 47]. Density corresponding to the amino-terminal domains I/II (1-118) of one copy of λP, which had been poorly resolved in our earlier study [21], was sufficiently ordered to allow fitting of the model calculated by AlphaFold. We positioned this calculated amino-terminal alpha helical domains I/II against only one chain of λP, i.e., chain Z (2:118). Both the amino terminal domain helices were moved

substantially into the EM density by Coot [30, 31]. AlphaFold predicted Domain I to be a straight helix, however, this conformation did not comport with our EM map, and hence the helix had to be bent after Asn-10.

To revise the C-terminal domains of λP in the BP complex, we manually positioned five copies of the carboxy terminal linker (residues 192:210), and Domain IV (residues 211:226) from the AlphaFold calculated model into our EM map; this procedure required that we significantly adjust the relative orientation of the linker and C-terminal helix. The final seven residues (227:233) of λP were positioned by superimposing the AlphaFold calculated model on the previously positioned C-terminal lasso/grappling hook helix, followed by manual adjustment to fit the density map. Notably, considerable adjustment of the relative orientation of the four domains in the AlphaFold calculated structure was required for fitting into our map. Our map also showed features that may correspond to one additional amino-terminal domain, however, the corresponding domains of the remaining copies of λP feature no density for this domain. Hence, the final BP model (PDB: TBD) encompasses residues DnaB (chain A- 27:169 and 201:468, chain B- 17:466, chain C- 19:471, chain D- 17:471, chain E- 20-471, and chain F- 23:468) and λP (chain V- 119:233, chain W- 119:232, chain X- 119:232, chain Y- 119:233, and chain Z- 2:233). Our model also included 5 ADP molecules bound to 5 magnesium ions bound to five of the DnaB chains: A, C, D, E, and F, chain B lacked any nucleotide.

Model analysis

Once the full BP model was generated, the model was manually inspected with for each of the amino acid residue with COOT and subjected to global Real Space Refinement with PHENIX [29, 48] (Figures were generated using UCSF-CHIMERA [47] and PYMOL [32].

Acknowledgments

This work was supported by the National Science Foundation (DJ: MCB 1818255), the National Institutes of Health (DJ: GM08416 and BTC: GM109824), and the Department of Education (JC: PA200A150068). We dedicate our work on the DnaB – λP complex to the memory of Professor Roger McMacken on whose shoulders we stand as we do our work and who inspired us in so many ways.

References

1. Yao N, O'Donnell M (2016) Bacterial and Eukaryotic Replisome Machines. *JSM biochemistry and molecular biology*, 3(1)

2. Yao NY, O'Donnell ME (2016) Evolution of replication machines. *Critical Reviews in Biochemistry and Molecular Biology*, 51(3):135–149. https://doi.org/10.3109/10409238.2015.1125845

3. MacNeill SA (2011) Protein-protein interactions in the archaeal core replisome. *Biochemical Society transactions*, 39(1):163–168. https://doi.org/10.1042/bst0390163

4. Kaguni JM (2014) DnaA, DnaB, and DnaC. :1–14. https://doi.org/10.1007/978-1-4614-6436-5_142-1

5. Velten M, McGovern S, Marsin S, Ehrlich SD, Noirot P, Polard P (2003) A Two-Protein Strategy for the Functional Loading of a Cellular Replicative DNA Helicase. *Molecular Cell*, 11(4):1009–1020. https://doi.org/10.1016/s1097-2765(03)00130-8

6. Brézellec P, Vallet-Gely I, Possoz C, Quevillon-Cheruel S, Ferat J-L (2016) DciA is an ancestral replicative helicase operator essential for bacterial replication initiation. *Nature communications*, 7:13271. https://doi.org/10.1038/ncomms13271

7. Brézellec P, Petit M-A, Pasek S, Vallet-Gely I, Possoz C, Ferat J-L (2017) Domestication of lambda phage genes into a putative third type of Replicative Helicase Matchmaker. *Genome Biology and Evolution*, 9(6):1561–1566. https://doi.org/10.1093/gbe/evx111

8. Bleichert F, Botchan MR, Berger JM (2017) Mechanisms for initiating cellular DNA replication. *Science*, 355(6327):eaah6317. https://doi.org/10.1126/science.aah6317

9. Marsin S, Adam Y, Cargemel C, Andreani J, Baconnais S, Legrand P, Li de la Sierra-Gallay I, Humbert A, Aumont-Nicaise M, Velours C, Ochsenbein F, Durand D, Le Cam E, Walbott H, Possoz C, Quevillon-Cheruel S, Ferat J-L (2021) Study of the DnaB:DciA interplay reveals insights into the primary mode of loading of the bacterial replicative helicase. *Nucleic Acids Research*, :gkab463-. https://doi.org/10.1093/nar/gkab463

10. Wang G, Klein MG, Tokonzaba E, Zhang Y, Holden LG, Chen XS (2008) The structure of a DnaB-family replicative helicase and its interactions with primase.

Nature Structural & Molecular Biology, 15(1):94–100. https://doi.org/10.1038/nsmb1356

11. Strycharska MS, Arias-Palomo E, Lyubimov AY, Erzberger JP, O'Shea VL, Bustamante CJ, Berger JM (2013) Nucleotide and partner-protein control of bacterial replicative helicase structure and function. *Molecular Cell*, 52(6):844–854. https://doi.org/10.1016/j.molcel.2013.11.016

12. Bailey S, Eliason WK, Steitz TA (2007) Structure of hexameric DnaB helicase and its complex with a domain of DnaG primase. *Science (New York, NY)*, 318(5849):459–463. https://doi.org/10.1126/science.1147353

13. Itsathitphaisarn O, Wing RA, Eliason WK, Wang J, Steitz TA (2012) The hexameric helicase DnaB adopts a nonplanar conformation during translocation. *Cell*, 151(2):267–277. https://doi.org/10.1016/j.cell.2012.09.014

14. Kaguni JM (2018) The Macromolecular Machines that Duplicate the Escherichia coli Chromosome as Targets for Drug Discovery. *Antibiotics*, 7(1):23. https://doi.org/10.3390/antibiotics7010023

15. Chodavarapu S, Kaguni JM (2016) Replication Initiation in Bacteria. 39:1–30. https://doi.org/10.1016/bs.enz.2016.03.001

16. O'Donnell M, Langston L, Stillman B (2013) Principles and concepts of DNA replication in bacteria, archaea, and eukarya. *Cold Spring Harbor perspectives in biology*, 5(7):a010108–a010108. https://doi.org/10.1101/cshperspect.a010108

17. Davey MJ, O'Donnell M (2003) Replicative helicase loaders: ring breakers and ring makers. *Current biology : CB*, 13(15):R594-6. https://doi.org/10.1016/s0960-9822(03)00523-2

18. O'Shea VL, Berger JM (2014) Loading strategies of ring-shaped nucleic acid translocases and helicases. *Current Opinion in Structural Biology*, 25:16–24. https://doi.org/10.1016/j.sbi.2013.11.006

19. Arias-Palomo E, Puri N, Murray VLO, Yan Q, Berger JM (2019) Physical Basis for the Loading of a Bacterial Replicative Helicase onto DNA. *Molecular Cell*, 74(1):173-184.e4. https://doi.org/10.1016/j.molcel.2019.01.023

20. Arias-Palomo E, O'Shea VL, Hood IV, Berger JM (2013) The Bacterial DnaC Helicase Loader Is a DnaB Ring Breaker. *Cell*, 153(2):438–448. https://doi.org/10.1016/j.cell.2013.03.006

21. Chase J, Catalano A, Noble AJ, Eng ET, Olinares PD, Molloy K, Pakotiprapha D, Samuels M, Chait B, Georges AD, Jeruzalmi D (2018)

Mechanisms of opening and closing of the bacterial replicative helicase. *eLife*, 7:1822. https://doi.org/10.7554/elife.41140

22. Chase J, Berger J, Jeruzalmi D (2022) Convergent evolution in two bacterial replicative helicase loaders. *Trends in Biochemical Sciences*, 47(7):620–630. https://doi.org/10.1016/j.tibs.2022.02.005

23. Jumper J, Evans R, Pritzel A, Green T, Figurnov M, Ronneberger O, Tunyasuvunakool K, Bates R, Žídek A, Potapenko A, Bridgland A, Meyer C, Kohl SAA, Ballard AJ, Cowie A, Romera-Paredes B, Nikolov S, Jain R, Adler J, Back T, Petersen S, Reiman D, Clancy E, Zielinski M, Steinegger M, Pacholska M, Berghammer T, Bodenstein S, Silver D, Vinyals O, Senior AW, Kavukcuoglu K, Kohli P, Hassabis D (2021) Highly accurate protein structure prediction with AlphaFold. *Nature*, 596(7873):583–589. https://doi.org/10.1038/s41586-021-03819-2

24. Varadi M, Anyango S, Deshpande M, Nair S, Natassia C, Yordanova G, Yuan D, Stroe O, Wood G, Laydon A, Žídek A, Green T, Tunyasuvunakool K, Petersen S, Jumper J, Clancy E, Green R, Vora A, Lutfi M, Figurnov M, Cowie A, Hobbs N, Kohli P, Kleywegt G, Birney E, Hassabis D, Velankar S (2021) AlphaFold Protein Structure Database: massively expanding the structural coverage of protein-sequence space with high-accuracy models. *Nucleic Acids Research*, 50(D1):D439–D444. https://doi.org/10.1093/nar/gkab1061

25. Mallory JB, Alfano C, McMacken R (1990) Host virus interactions in the initiation of bacteriophage lambda DNA replication. Recruitment of Escherichia coli DnaB helicase by lambda P replication protein. *The Journal of biological chemistry*, 265(22):13297–13307.

26. Orlova N, Gerding M, Ivashkiv O, Olinares PDB, Chait BT, Waldor MK, Jeruzalmi D (2017) The replication initiator of the cholera pathogen's second chromosome shows structural similarity to plasmid initiators. *Nucleic Acids Research*, 45(7):3724–3737. https://doi.org/10.1093/nar/gkw1288

27. Kantardjieff KA, Rupp B (2003) Matthews coefficient probabilities: Improved estimates for unit cell contents of proteins, DNA, and protein-nucleic acid complex crystals. *Protein science : a publication of the Protein Society*, 12(9):1865–1871. https://doi.org/10.1110/ps.0350503

28. Otwinowski Z, Minor W (1997) Processing of X-ray diffraction data collected in oscillation mode. *Macromolecular Crystallography, Pt A*, 276:307–326.

29. Liebschner D, Afonine PV, Baker ML, Bunkóczi G, Chen VB, Croll TI, Hintze B, Hung LW, Jain S, McCoy AJ, Moriarty NW, Oeffner RD, Poon BK, Prisant MG, Read RJ, Richardson JS, Richardson DC, Sammito MD, Sobolev OV, Stockwell DH, Terwilliger TC, Urzhumtsev AG, Videau LL, Williams CJ, Adams PD (2019)

Macromolecular structure determination using X-rays, neutrons and electrons: recent developments in Phenix. *Acta Crystallographica Section D: Structural Biology*, 75(10):861–877. https://doi.org/10.1107/s2059798319011471

30. Brown A, Long F, Nicholls RA, Toots J, Emsley P, Murshudov G (2015) Tools for macromolecular model building and refinement into electron cryo-microscopy reconstructions. *Acta crystallographica Section D, Biological crystallography*, 71(1):136–153. https://doi.org/10.1107/s1399004714021683

31. Emsley P, Cowtan K (2004) Coot: model-building tools for molecular graphics. *Acta crystallographica Section D, Biological crystallography*, 60(Pt 12 Pt 1):2126–2132. https://doi.org/10.1107/s0907444904019158

32. LLC S , (2017) The PyMOL Molecular Graphics System, Version 2.1.

33. Learn BA, Um SJ, Huang L, McMacken R (1997) Cryptic single-stranded-DNA binding activities of the phage lambda P and Escherichia coli DnaC replication initiation proteins facilitate the transfer of E. coli DnaB helicase onto DNA. *Proceedings of the National Academy of Sciences of the United States of America*, 94(4):1154–1159. https://doi.org/10.1073/pnas.94.4.1154

34. Suloway C, Pulokas J, Fellmann D, Cheng A, Guerra F, Quispe J, Stagg S, Potter CS, Carragher B (2005) Automated molecular microscopy: the new Leginon system. *Journal of structural biology*, 151(1):41–60. https://doi.org/10.1016/j.jsb.2005.03.010

35. Noble AJ, Dandey VP, Wei H, Braschi J, Chase J, Acharya P, Tan YZ, Zhang Z, Kim LY, Scapin G, Rapp M, Eng ET, Rice WJ, Cheng A, Negro CJ, Shapiro L, Kwong PD, Jeruzalmi D, Georges AD, Potter CS, Carragher B (2018) Routine single particle cryoEM sample and grid characterization by tomography. *eLife*, 7https://doi.org/10.7554/elife.34257

36. Tegunov D, Cramer P (2019) Real-time cryo-electron microscopy data preprocessing with Warp. *Nature Methods*, 16(11):1146–1152. https://doi.org/10.1038/s41592-019-0580-y

37. Punjani A, Zhang H, Fleet DJ (2020) Non-uniform refinement: adaptive regularization improves single-particle cryo-EM reconstruction. *Nature Methods*, 17(12):1214–1221. https://doi.org/10.1038/s41592-020-00990-8

38. Punjani A, Fleet DJ (2021) 3D variability analysis: Resolving continuous flexibility and discrete heterogeneity from single particle cryo-EM. *Journal of Structural Biology*, 213(2):107702. https://doi.org/10.1016/j.jsb.2021.107702

39. Punjani A, Rubinstein JL, Fleet DJ, Brubaker MA (2017) cryoSPARC: algorithms for rapid unsupervised cryo-EM structure determination. *Nature Methods*, 14(3):290–296. https://doi.org/10.1038/nmeth.4169

40. Sanchez-Garcia R, Gomez-Blanco J, Cuervo A, Carazo JM, Sorzano COS, Vargas J (2021) DeepEMhancer: a deep learning solution for cryo-EM volume post-processing. *Communications Biology*, 4(1):874. https://doi.org/10.1038/s42003-021-02399-1

41. Henderson R, Sali A, Baker ML, Carragher B, Devkota B, Downing KH, Egelman EH, Feng Z, Frank J, Grigorieff N, Jiang W, Ludtke SJ, Medalia O, Penczek PA, Rosenthal PB, Rossmann MG, Schmid MF, Schröder GF, Steven AC, Stokes DL, Westbrook JD, Wriggers W, Yang H, Young J, Berman HM, Chiu W, Kleywegt GJ, Lawson CL (2012) Outcome of the First Electron Microscopy Validation Task Force Meeting. *Structure/Folding and Design*, 20(2):205–214. https://doi.org/10.1016/j.str.2011.12.014

42. Rosenthal PB, Rubinstein JL (2015) Validating maps from single particle electron cryomicroscopy. *Current Opinion in Structural Biology*, 34:135–144. https://doi.org/10.1016/j.sbi.2015.07.002

43. Vagin A, Teplyakov A (2010) Molecular replacement with MOLREP. *Acta crystallographica Section D, Biological crystallography*, 66(Pt 1):22–25. https://doi.org/10.1107/s0907444909042589

44. Vagin AA, Isupov MN (2001) Spherically averaged phased translation function and its application to the search for molecules and fragments in electron-density maps. *Acta crystallographica Section D, Biological crystallography*, 57(Pt 10):1451–1456.

45. Vagin A, Teplyakov A (2000) An approach to multi-copy search in molecular replacement. *Acta crystallographica Section D, Biological crystallography*, 56(Pt 12):1622–1624.

46. Winn MD, Ballard CC, Cowtan KD, Dodson EJ, Emsley P, Evans PR, Keegan RM, Krissinel EB, Leslie AGW, McCoy A, McNicholas SJ, Murshudov GN, Pannu NS, Potterton EA, Powell HR, Read RJ, Vagin A, Wilson KS (2011) Overview of the CCP4 suite and current developments. *Acta crystallographica Section D, Biological crystallography*, 67(Pt 4):235–242. https://doi.org/10.1107/s0907444910045749

47. Pettersen EF, Goddard TD, Huang CC, Couch GS, Greenblatt DM, Meng EC, Ferrin TE (2004) UCSF Chimera--a visualization system for exploratory research and analysis. *Journal of computational chemistry*, 25(13):1605–1612. https://doi.org/10.1002/jcc.20084

48. Afonine PV, Poon BK, Read RJ, Sobolev OV, Terwilliger TC, Urzhumtsev A, Adams PD (2018) Real-space refinement in PHENIX for cryo-EM and crystallography. *Acta Crystallographica Section D: Structural Biology*, 74(Pt 6):531–544. https://www.ncbi.nlm.nih.gov/pubmed/29872004

Figures/Figure legends

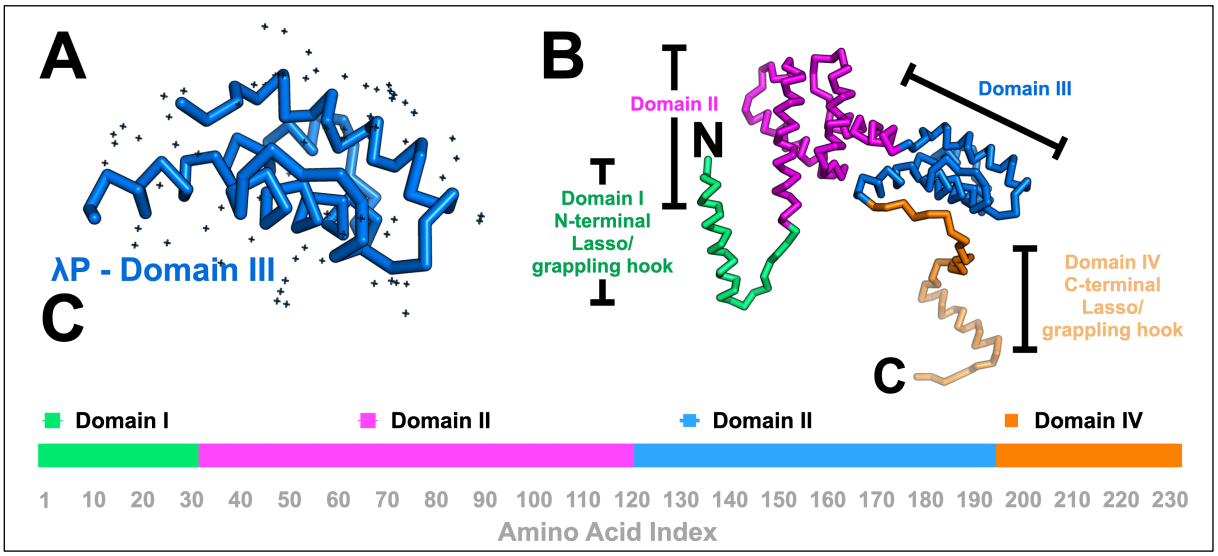

Figure 1. The Complete Structure of the λP Helicase Loader. A) 1.86 Å crystal structure of domain III. The observed water molecules are shown as plus (+) signs. B) The Alphafold calculated model. C) Linear domain map of λP.

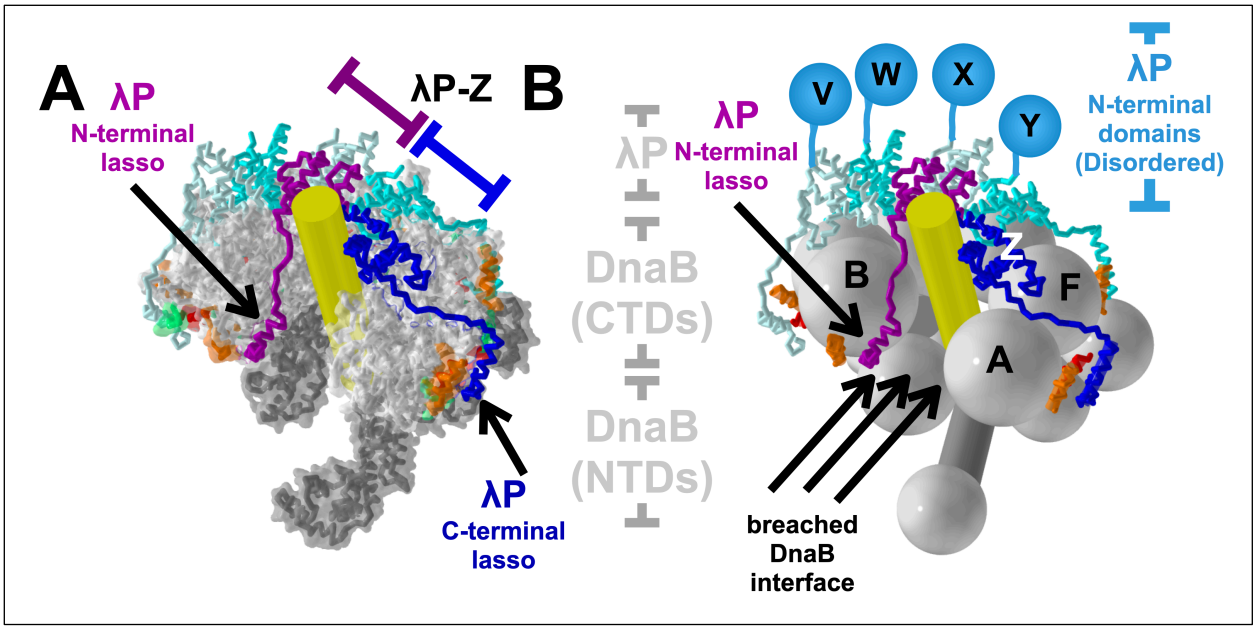

Figure 2. The Structure of the DnaB – λP loader. A) The five λP loader molecules are depicted in the ribbon representation and colored in shades of blue. The complete structure of λP chain Z is modeled and depicted colored in magenta. The right-handed open spiral of DnaB is depicted in the ribbon representation along with a transparent surface. The yellow cylinder represents the expected path of ssDNA as inferred from comparison to the DnaB•DnaC-ssDNA complex (PDB: 6QEM). B) Same as panel A, except that the NTD and CTD layers of DnaB are depicted using large spheres (CTD) and small spheres/cylinder (NTD).

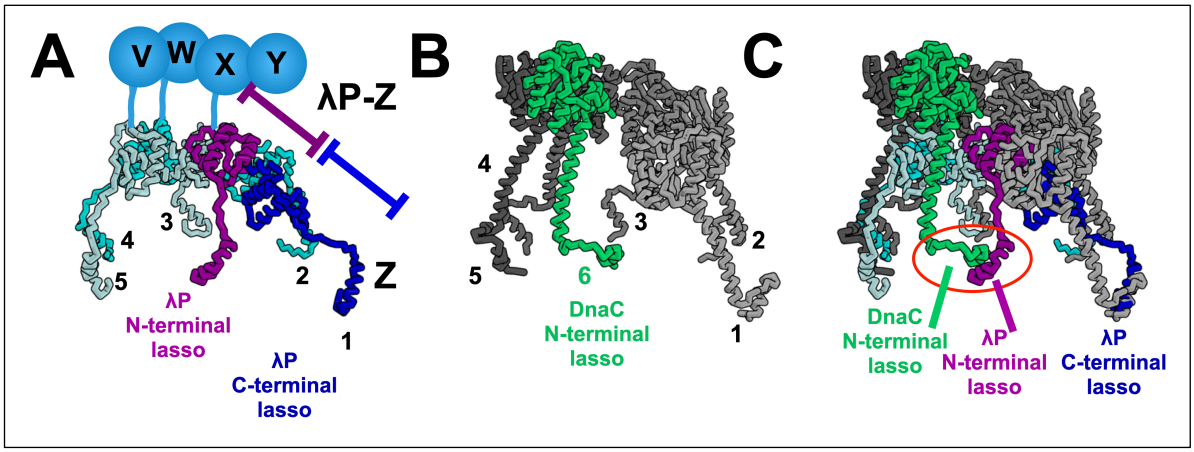

Figure 3. Comparison of the λP and DnaC loader ensembles. A) The pentameric λP; the four disordered N-terminal domains are depicted with spheres; each λP loader subunit is numbered and labeled with its chain identifier; B) the hexameric DnaC loaders; each DnaC loader subunit is numbered; C) Superposition of the λP and DnaC loaders. The BP and BC complexes were superimposed on the CTD domain of the DnaB subunit at the bottom of the spiral. For clarity, the superimposed DnaB spirals are not shown. Each of the C-terminal lassos from λP superimposes on a DnaC lasso. However, the single visible N-terminal lasso overlaps with the position of the DnaC lasso at the top of the spiral.

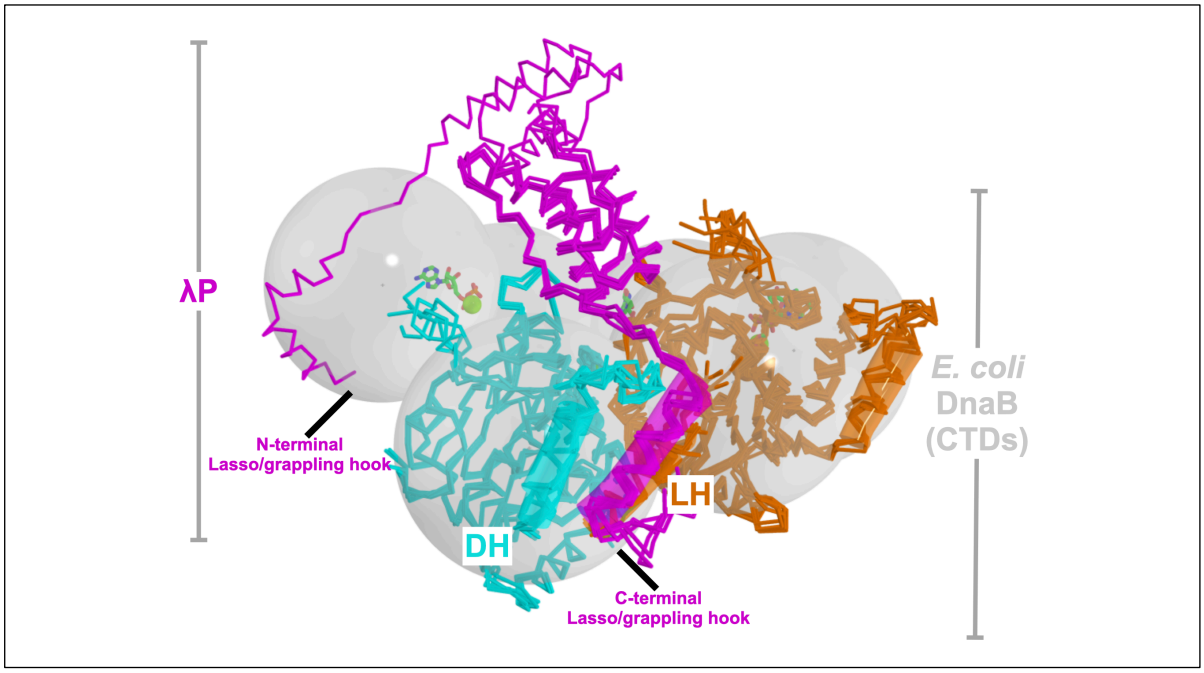

Figure 4. Superposition of the Five DnaB – λP Interfaces. Each instance of the B_2P_1 sub-structure was superimposed on the 'left' DnaB subunit, as in the frame of reference provided by this pose. The superposition calculation included residues 206 to 289 and 307 to 471; residues that correspond to the LH element (181-196) and the DH element (290-306) were excluded. The 'left' DnaB subunit after superposition is colored in cyan and the 'right' subunit is colored in orange. Each of the five λP chains are colored in magenta. The root mean square deviations of the superpositions ranged from 0.61 to 0.67 Å on 246 Cα atoms.

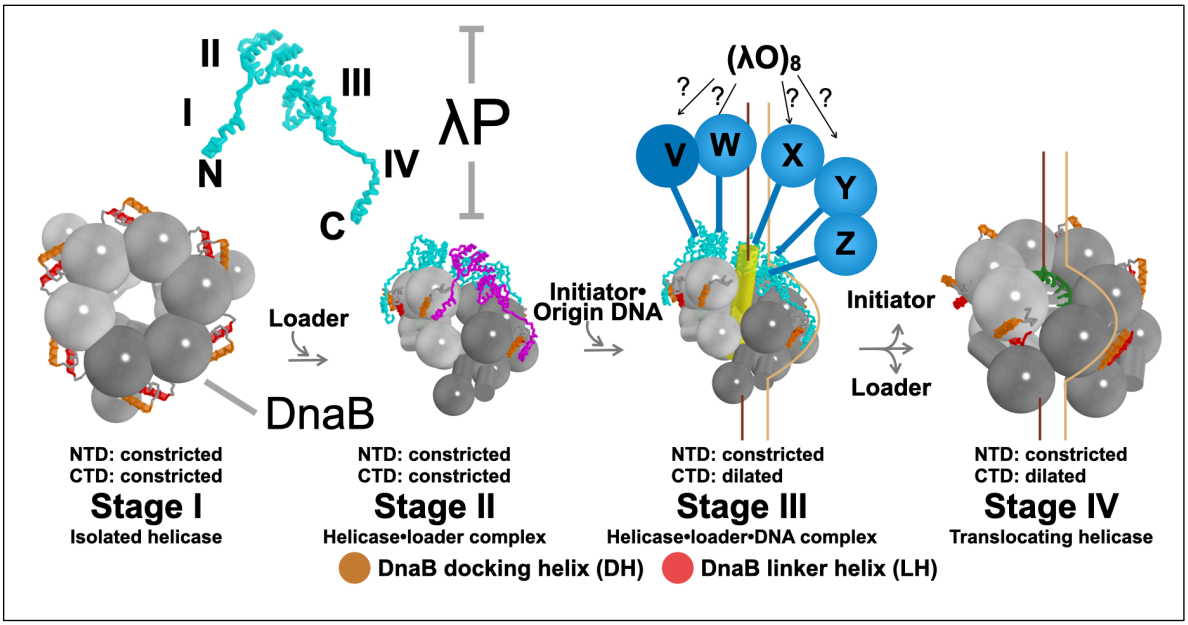

Figure 5. Model for Loading of the DnaB-λP loader complex to the λO-Oriλ.

Details are provided in the main text.

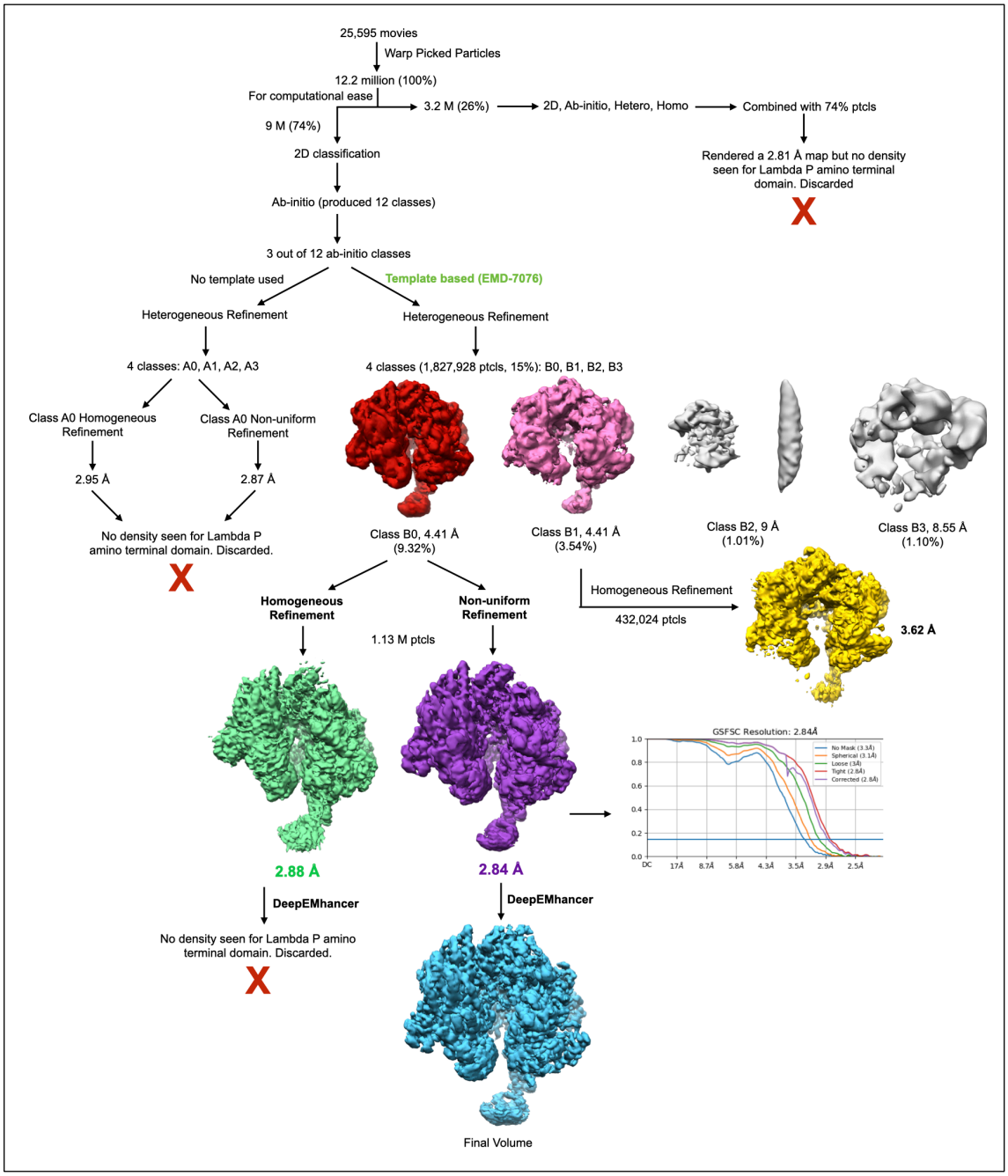

Figure S1: Cryo-EM Data-Processing for the E.coli DnaB – λP Complex. ~25K movies were collected and passed through CTF estimation, motion correction, and particle picking with WARP as described in the text. This was followed by 2D and 3D classification that produced 3 good classes with ~1.8 million particles. These ~1.8 million particles went through heterogeneous refinement and produced 4

classes: B0, B1, B2, and B3. Particles in class B0 comprising 9.32% of the complete set of picked particles were further refined in two ways: homogeneous refinement which produced a 2.88 Å map (green) and non-uniform refinement which yielded a 2.84 Å map (purple). The 2.84 Å map was submitted to the DeepEMhancer software for sharpening; this procedure produced the final map (cyan).